Astronomy & Astrophysics manuscript no. vbls5039
March 19, 2007

Exploring the connection between the stellar wind and the non-thermal emission in LS 5039⋆

V. Bosch-Ramon[1], C. Motch[2], M. Ribó[3], R. Lopes de Oliveira[2,4], E. Janot-Pacheco[4], I. Negueruela[5], J. M. Paredes[3], and A. Martocchia[6]

[1] Max Planck Institut für Kernphysik, Saupfercheckweg 1, Heidelberg 69117, Germany; vbosch@mpi-hd.mpg.de
[2] Observatoire Astronomique, rue de l'Universite 11, Strasbourg 67000, France; motch@astro.u-strasbg.fr
[3] Departament d'Astronomia i Meteorologia, Universitat de Barcelona, c/Martí i Franquès 1, 08028 Barcelona, Catalonia, Spain; mribo@am.ub.es, jmparedes@ub.edu
[4] Universidade de São Paulo, Instituto de Astronomia, Geofísica e Ciências Atmosféricas - IAG, Departamento de Astronomia, Rua do Matão, 1226 - 05508-900 São Paulo, Brazil; rlopes@astro.iag.usp.br, janot@astro.iag.usp.br
[5] Dpto. de Física, Ingeniería de Sistemas y Teoría de la Señal, Universidad de Alicante, Apdo. 99, 03080 Alicante, Spain: ignacio@dfists.ua.es
[6] Istituto Nazionale di Astrofisica, Via del Fosso del Cavaliere 100, 00133 Roma, Italy; andrea.martocchia@iasf-roma.inaf.it

Preprint online version: March 19, 2007

ABSTRACT

Context. The gamma-ray microquasar LS 5039 has been observed with several X-ray instruments so far, presenting variability of likely orbital origin in flux and photon index but no signatures of accretion disk. In addition, this system harbors an O-type star with relatively strong mass loss. At present, a global picture to explain the non-thermal emission, and the possible impact of the stellar wind on the former, is still missing.
Aims. We study here the X-ray fluxes, spectra, and absorption properties of LS 5039 at apastron and periastron passages, and their possible association with the stellar wind state, inferred from Hα line equivalent width (EW) data. The physical link between the stellar wind and the multiwavelength non-thermal emission is also explored.
Methods. New *XMM-Newton* observations have been performed around periastron and apastron passages in September 2005, during an epoch of presumably enhanced O star wind. Also, 2005 *Chandra* observations on LS 5039 are revisited. Moreover, a compilation of the Hα EW and *RXTE*/ASM X-ray count rate obtained since the 1990s is carried out, being both quantities compared with each other and also with historical radio data.
Results. *XMM-Newton* observations show higher and harder emission around apastron than around periastron. No signatures of thermal emission or a reflection iron line indicating the presence of an accretion disk are found in the spectrum, and the hydrogen column density ($N_{\rm H}$) is compatible with being the same in both observations and consistent with the interstellar value. The hardness ratio ($\rm HR_{2-12/0.3-2\ keV}$) and the count rate seem uncorrelated at periastron and may be correlated at apastron. We find that LS 5039 was bright and hard in 2005 *Chandra* observations. The ASM count rate shows changes by a $\sim 80\%$ on year timescales, and the Hα EW shows yearly variations of a $\sim 10\%$. Both quantities may be anticorrelated rather than correlated, unlike it was previously thought. At radio frequencies, the emission varies by $\sim 20\%$, presenting some similarities with the X-ray evolution. ASM, Hα EW and radio data may hint to variability at orbital timescales.
Conclusions. 2005 *XMM-Newton* and *Chandra* observations seem to confirm 2003 *RXTE*/PCA results, namely moderate flux and spectral variability at orbital and shorter timescales. The low value and constancy of the $N_{\rm H}$ could imply that the X-ray emitter is located at $\gtrsim 10^{12}$ cm from the compact object. We suggest that the multiwavelength non-thermal emission produced in LS 5039 is related to the jet and the stellar wind in a rather complex way and mostly produced outside the binary system. However, the present data do not rule out the young pulsar scenario.

Key words. X-rays: binaries – stars: individual: LS 5039 – Radiation mechanisms: non-thermal

1. Introduction

LS 5039 is an X-ray binary (Motch et al. 1997) located at 2.5±0.5 kpc (Casares et al. 2005; C05 hereafter). The source presents radio jets (Paredes et al. 2000, 2002), shows X-ray variability on timescales similar to the orbital one (Bosch-Ramon et al. 2005; BR05 hereafter), and has been detected at very high-energy (VHE) gamma-rays (Aharonian et al. 2005), which virtually confirms its association with a *CGRO*/EGRET (EGRET from now on) source (Paredes et al. 2000). The orbital ephemeris of the system were obtained by C05 and are

Send offprint requests to:
e-mail: vbosch@mpi-hd.mpg.de

⋆ The Hα results presented here are based on observations made with ESO Telescopes at the La Silla or Paranal Observatories under program IDs 67.D-0229(A), 69.D-0628(A) and 075.D-0591(A); the Observatoire de Haute-Provence; the Observatório do Pico dos Dias / LNA, Brazil; the G.D. Cassini telescope operated at the Loiano Observatory by the Osservatorio Astronómico di Bologna; and the Nordic Optical Telescope, operated on the island of La Palma jointly by Denmark, Finland, Iceland, Norway, and Sweden, in the Spanish Observatorio del Roque de los Muchachos of the Instituto de Astrofisica de Canarias (those data were taken using ALFOSC, which is owned by the Instituto de Astrofísica de Andalucía (IAA) and operated at the Nordic Optical Telescope under agreement between IAA and the NBIfAFG of the Astronomical Observatory of Copenhagen).

T_0 = HJD 2451943.09, for the time of the periastron passage (phase 0.0), $P_{\rm orb}$ = 3.90603 ± 0.00017 days, for the orbital period, and e = 0.35 ± 0.04, for the eccentricity of the system; the inclination is constrained to $i \sim 15^\circ$–60°. Interestingly, the TeV emission varies with the orbital period (Aharonian et al. 2006). Recently, LS 5039 has been also detected by *INTEGRAL* (Goldoni et al. 2006) up to 100 keV (De Rosa et al. 2006). In addition, LS 5039 is also the likely counterpart of a *CGRO*/COMPTEL (COMPTEL from now on) source (Strong et al. 2001; Collmar 2003). The nature of the compact object is still uncertain. C05 suggest that it may be a black hole, although there is an on-going debate on this issue, and some authors have proposed that LS 5039 is in fact a young non-accreting pulsar (see, e.g., Martocchia et al. 2005; Dubus 2006; and Sect. 5).

Radio emission is non-thermal, slightly variable at month–year timescales (∼ 20–30%) and extended -∼1 – 100 milliarcseconds (mas)- (Martí et al. 1998; Ribó et al. 1999; Paredes et al. 2000, 2002; for an exhaustive study, see Ribó 2002), the ∼ 60–80% being produced within a core of ∼ mas. It is worth noting that, in fact, if all the observed variability were originated in the source core, the radio emission produced there could vary up to a 50%.

All the X-ray observations performed by instruments with imaging capabilities have not shown strong variations of flux and photon index (for a compilation, see below). Data taken by *RXTE*/PCA (*RXTE* from now on), which does not produce images but integrates all the detected photons in a $\sim 1^\circ \times 1^\circ$ field of view, showed significantly softer spectra and larger fluxes than the other observations, and evidence of the presence of an iron K_α line (e.g. Ribó et al. 1999), although now we know that these results are likely due to contamination by diffuse X-ray emission coming from the Galactic Ridge (BR05). Despite this, 2003 *RXTE* data showed variations of the flux (a factor of ∼ 2) and spectral index that are of likely orbital origin, with the emission peaking and the spectrum hardening smoothly around phase 0.8 and more sharply at other phases (BR05). A possible relationship between the mass-loss rate of the companion star and the X-ray emission in LS 5039 was discussed in previous works and a correlation suggested in the context of wind accretion powering the X-rays (e.g., Reig et al. 2003; McSwain et al. 2004), although the amount of data was limited precluding conclusive results.

At MeV-GeV energies, data are dim and do not allow for a study of the time evolution. However, we note that the EGRET source associated to LS 5039 may be variable (Torres et al. 2001).

At VHE, the flux and the photon index change periodically, by a factor of ∼ 2.5 the former and between ∼ 1.9–3.1 the latter, with the spectrum hardening when flux increases (Aharonian et al. 2006). The maximum of the emission takes place around phase 0.8, similarly as it seems to happen at X-rays. Also, sudden increases/hardening in the flux and spectrum on hour timescales could have been detected at phase ∼0.85 (de Naurois et al. 2006). Simultaneous *Chandra* observations, reanalyzed here, presented also a very hard and high X-ray emission (Horns et al. 2006).

In this work, we present recent *XMM-Newton* observations of LS 5039 carried out in September 2005 during periastron and apastron passages, in an epoch of inferred high stellar mass-loss rate. *Chandra* data, taken in the same year and during the orbital phase ≈ 0.85, when *RXTE* showed a smooth peak of the X-ray emission, are reanalyzed. We analyze also the long-term and orbital Hα EW evolution, linked to the evolution of the stellar mass-loss rate, and compare it with 1996–2006 *RXTE*/ASM (ASM from now on) data, since in the standard wind accretion scenario an enhancement of the stellar mass-loss rate would be expected to be linked to an increase in the X-ray emission. Historical Green Bank Interferometer (GBI) data are also revisited. These results at different wavelengths, accounting also for VHE data, are put in context, and a physical scenario is proposed.

Table 1. Date, initial and final HJD times, observation identification number (OBSID) of the *XMM-Newton* observations, and orbital phase (ephemeris taken from C05).

Date	$\rm HJD_{start}$–$\rm HJD_{stop}$	OBSID	Orbital phase
2005-09-22	2453636.214–2453636.397	0202950201	0.49–0.53
2005-09-24	2453638.279–2453638.399	0202950301	0.02–0.05

2. X-ray observations

2.1. *XMM-Newton* observations

The *XMM-Newton* observations presented here were performed in two runs, the 22th and 24th of September 2005, with EPIC pn on times of 15.8 ks and 10.4 ks (very similar to those of MOS1 and MOS2), respectively (see Table 1). The corresponding observed phases are 0.49–0.53, around apastron, and 0.02–0.05, right after periastron. These observations were triggered in the context of a target of opportunity (ToO) program linked to the strength of the Hα line, which gives information on the state of the stellar wind. The Hα EW was found in late August 2005 to be above of −2.4Å, defined as the threshold set to trigger the *XMM-Newton* observations and significantly larger than the values observed during the previous years. The *XMM-Newton* observations presented here were carried out in September due to visibility constraints. The physical motivation of the ToO was that, if direct accretion of the stellar wind is taking place in the system, the detection of X-ray accretion features like a multicolor black-body or a reflection iron line seems more likely during epochs of larger stellar mass loss and thereby higher accretion rate. The convention for the Hα EW in this work is to take this value as negative when in absorption, i.e. it increases in the same sense as the stellar mass-loss rate.

We focus here on the data obtained with the EPIC instrument, since the X-ray spectrometer (RGS) data did not have enough statistics due to the faintness of the source. The MOS and pn cameras were in small and full window respectively, with medium filters. The reduction and analysis of the data have been performed following the standard procedure using the SAS 7.0.0 software package to filter data and create spectra and lightcurves, and Xspec 12.3.0 for the spectral analysis. No large background flare was present any of the two data sets. The 0.3–12 keV count rates per camera around phases 0.5 and 0.0 were 0.46 and 0.29 cts $\rm s^{-1}$ for MOS1, 0.47 and 0.30 cts $\rm s^{-1}$ for MOS2, and 1.09 and 0.71 cts $\rm s^{-1}$ for pn, respectively.

The lightcurves and the $\rm HR_{2-12/0.3-2\ keV}$ evolution, adding the data from pn, MOS1 and MOS2 cameras and taking time bins of 500 s, are presented in Figs. 1 and 2 for apastron and periastron passage, respectively. Around apastron, the emission is variable on timescales of a few hours. A constant fit to the data gives a reduced χ squared ($\chi^2_{\rm red}$) of 6.8, and the maximum count rate variation is ≈ 25% during this run, with deviations of $\approx \pm 5\sigma$ from the mean value. At intra-hour scales, the count rate varies by a ≈ 20% (4σ) between time bins separated by ∼1000 s

(at 10000 s from the beginning of the run; see Fig. 1, bottom). Around periastron, the lightcurve is still somewhat inconsistent with being constant ($\chi^2_{\rm red}$ = 2.4), with a maximum count rate variation of $\approx$ 25% and deviations of $\approx \pm 2\sigma$ from the mean value. For both runs, the $HR_{2-12/0.3-2\ keV}$ is compatible with being constant, although the $\chi_{\rm red}$ is worse (1.4) for the apastron than for the periastron run (1). Despite this, we looked for correlations between the count rate and the $HR_{2-12/0.3-2\ keV}$, finding some hints around apastron (linear correlation coefficient r of 0.5), but not around periastron (r = 0.2). It seems that the source is more variable during the apastron, when the count rate and the $HR_{2-12/0.3-2\ keV}$ are also higher and there might be correlation, although these differences may be due to the worse statistics of periastron data.

In order to search for pulsations, we applied the Z^2_n (Rayleigh) test (see, e.g., Zavlin et al. 2000) to the EPIC pn data which were acquired in the PrimeSmallWindow mode with a time resolution of 6 ms. In the frequency range of 0.01 to 83 Hz, no significant period peaks are found, and the pulsed fraction has been constrained to be less than 8% (apastron) and 11.3% (periastron). Similar upper-limits are reported by Martocchia et al. (2005) for 2003 *XMM-Newton* data. We show in Fig. 3 the spectrum of the source around phase 0.5, altogether with the deviations in σ of the best fit model from the data. We have added the data obtained from the pn, MOS1 and MOS2 cameras. The spectrum around phase 0.0 is not shown though it looks very similar to the one around phase 0.5. The spectrum of the emission is well represented by an absorbed power-law ($\chi^2_{\rm red}$ = 1.08 and 0.93 for phases 0.5 and 0.0, respectively). The unabsorbed fluxes and photon indices (0.3–10 keV) are of $(1.18^{+0.03}_{0.07})\times10^{-11}$ erg cm^{-2} s^{-1} (8.8×10^{33} erg s^{-1}) and 1.50±0.02 around phase 0.5, and $(0.74 \pm 0.07) \times 10^{-11}$ erg cm^{-2} s^{-1} (5.6×10^{33} erg s^{-1}) and 1.58±0.03 around phase 0.0. The flux between periastron and apastron increases by a 60% at a level of 4.4σ, and the photon index rises up marginally by 0.08 (2.2σ). All the errors given here are 1 σ. For the absorption model, we used *phabs*, which assumes updated photoelectric cross-sections from Balucinska-Church & Mc Cammon (1992). The $N_{\rm H}$ values are compatible within errors between both runs, being $(6.3 \pm 0.1) \times 10^{21}$ cm^{-2} around phase 0.5 and $(6.2 \pm 0.2) \times 10^{21}$ cm^{-2} around phase 0.0. In fact, when computed with a *wabs* model, the $N_{\rm H}$ value around apastron is similar to those found by Martocchia et al. (2005) at similar orbital phases (see below).

A multi-color black-body (*bbody*) and a Gaussian line component were added, separately, to the absorbed power-law model for the two runs. Around apastron, we obtained a preferred temperature for the black-body around 1 keV, and a 3 σ flux upper-limit of about a 10% the total one, derived from normalizing the black-body to three times its error ($\chi^2_{\rm red}$ from 1.1 to 2.0). At the same phase, we tried to fit a possible iron line with a Gaussian model. We explored the energy region around 6.1–6.9 keV, fixing the line energy at different values, looking for upper-limits of the line flux. Using a line EW of 20 and 390 eV, the former being similar to the upper-limits found by Martocchia et al. (2005) for 2003 *XMM-Newton* data, and the latter being the value obtained by Ribó et al. (1999) from 1998 *RXTE* data, the derived line fluxes were consistent with zero. Taking as the line normalization its 3 σ error, we obtained an upper-limit for the flux of about a 2% the total one ($\chi^2_{\rm red}$ from 1.1 to 1.2). Similar results concerning the presence of a black-body or an iron line component were obtained for the run around periastron. The lack of a multi-color black-body and a line component in the data is consistent with previous observations and provides further evidence that the line detected by *RXTE* was a background feature (see also BR05).

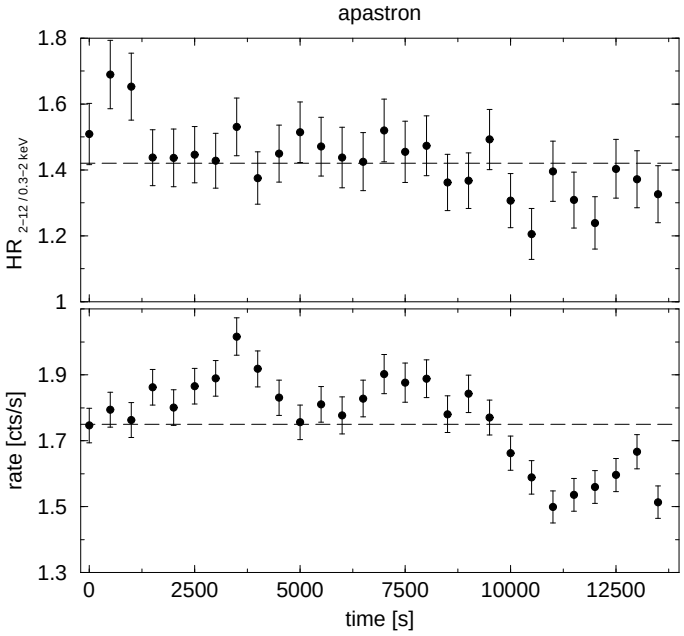

Fig. 1. Evolution of the $HR_{2-12/0.3-2\ keV}$ (top) and the count rate in the range 0.3–12 keV (bottom) during the observation taken around apastron passage. Data from the pn, MOS1 and MOS2 cameras have been used. The time bins are 500 s. For comparison, in both plots the mean value is given as long-dashed line.

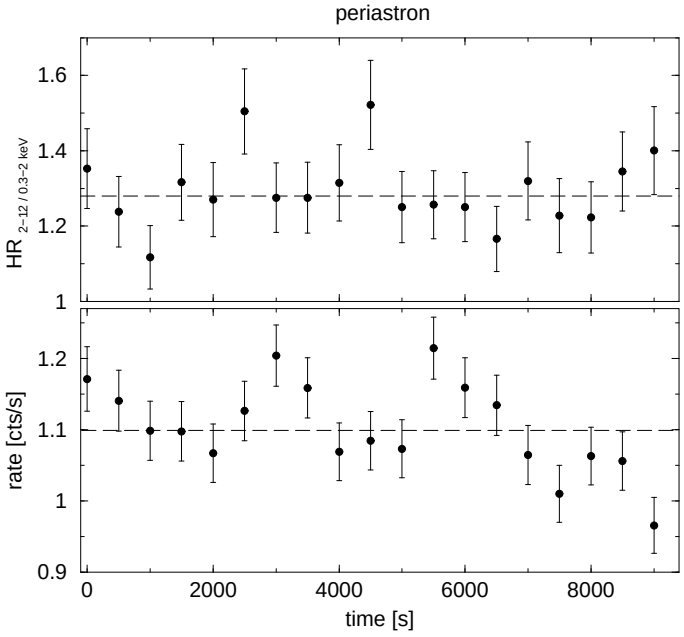

Fig. 2. The same as in Fig. 1 but around periastron passage.

To compare fluxes and spectra from other orbital phases, we also analyzed recent *Chandra* observations extracted from the archive (e.g. Horns et al. 2006). We note that an accurate comparison is precluded by the several months of difference between *XMM-Newton* and *Chandra* observations.

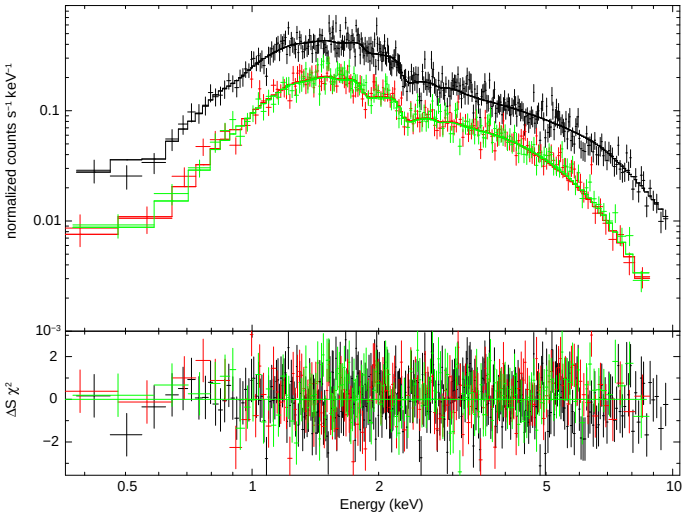

Fig. 3. Spectral data from pn (upper spectrum), MOS1 and MOS2 (lower spectra) cameras, and the best fit to the three of them: an absorbed power-law, around phase 0.5 (those around phase 0.0 look very similar and are not shown here). The deviations in σ of the model from the data are shown in the lower panel.

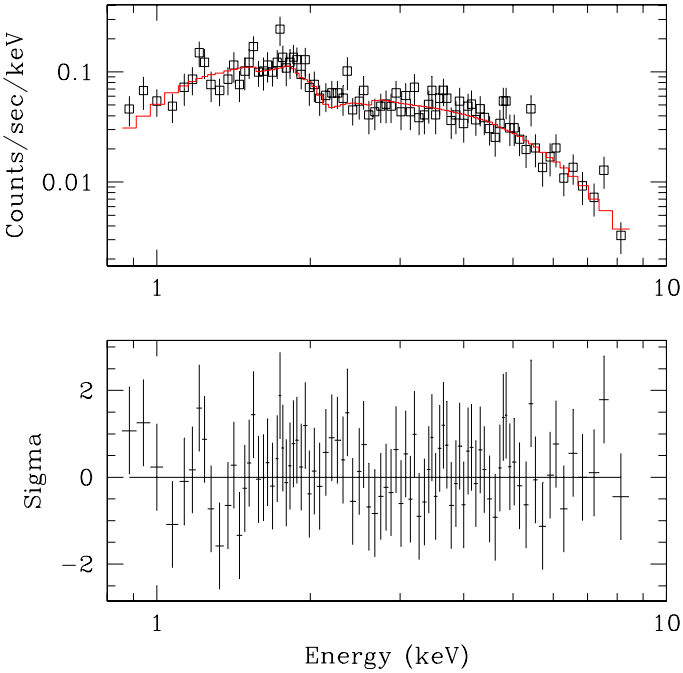

Fig. 4. At the top, the spectrum of the *Chandra* observation presented altogether with the fit using an absorbed power-law plus a pileup model. At the bottom, the deviations in σ of the data from the model are shown.

2.2. *Chandra* data

In April 2005, *Chandra* observed LS 5039 (HJD_{start}=2453473.616, HJD_{stop}=2453473.674) in the ACIS-S mode (time frame: 1.6 s) during 5 ks. It corresponds to the orbital phase 0.86–0.87, at which *RXTE* observed a smooth maximum (BR05). The *Chandra* Interactive Analysis of Observations software package (CIAO 3.3.0.1) has been used to extract the spectrum and the lightcurve, following the standard procedure given in the *Chandra* analysis threads. *Sherpa* (CIAO 3.3) has been used to analyze the spectrum. The ACIS count rate was relatively high, 0.3 cts s^{-1} (0.3–10 keV). *Chandra* data is likely moderately affected by pileup (see *The Chandra Proposers' Observatory Guide*, Fig. 6.19). Therefore, we have used the pileup model available in Sherpa to obtain our fits (Davis 2001).

The spectrum, presented in Fig. 4, can be well fitted by a power-law model with absorption (*xsphabs*) and pileup. We perform the spectral fit fixing the event pileup fraction parameter to 0.95 to avoid unreasonably high values for the flux (i.e. $\sim 10^{-10}$ erg cm^{-2} s^{-1}). We obtained a relatively low grade migration parameter of 0.2 ± 0.1. The pileup fraction is ∼ 11%. Therefore, the effect of pileup on these observations seems to be only moderate, as expected due to the relatively short time frame (1.6 s), which allows for a more efficient photon counting. The photon index is 1.1±0.2, and $N_{\rm H} = (6 \pm 1) \times 10^{21}$ cm^{-2}. To check the photon index value, we have calculated the spectrum without applying the pileup model after removing the central pixels (the most affected by pileup), obtaining compatible spectral parameter values. The 0.3–10 keV flux is $(2 \pm 1) \times 10^{-11}$ erg cm^{-2} s^{-1} (1.5×10^{34} erg s^{-1}). No disk or line components are required to fit the data. The lightcurve is quite noisy and (marginally) consistent with being constant (for a time bin of 100 s: $\chi^2_{\rm red} = 1.3$).

Despite the *Chandra* fitting results are somewhat loose, the source seems to be in an active and hard X-ray state. Although taken at different epochs and possibly affected by variability at longer timescales, the 2005 *XMM-Newton* and *Chandra* results are compatible with the lightcurve shown by 2003 *RXTE* data (BR05), which spans one orbital period and shows a maximum around phase 0.8. This favors the hypothesis that the X-ray variability of LS 5039 found in 2003 *RXTE* is of orbital origin.

For illustrative purposes, we show in Fig. 5 the 0.3–10 keV unabsorbed fluxes, photon indices and $N_{\rm H}$ (with *wabs* model) values obtained by all the previous imaging X-ray instruments that observed LS 5039. *ROSAT* and *RXTE* data are not included due to a low energy coverage and lack of imaging capabilities, respectively. These data are also presented in Table 2. Using the values provided in that table, we obtain the following weighted mean values for the 0.3–10 keV flux, $(1.05 \pm 0.02) \times 10^{-11}$ erg cm^{-2} s^{-1} (fit-to-constant $\chi^2_{\rm red} = 8.4$), the photon index, 1.54 ± 0.01 (fit-to-constant $\chi^2_{\rm red} = 2.7$), and $N_{\rm H}$, $(6.8 \pm 0.1) \times 10^{21}$ cm^{-2} (fit-to-constant $\chi^2_{\rm red} = 0.7$). Therefore, the flux found by all the instruments with imaging capabilities is clearly variable (even when excluding the 2005 *Chandra* data point), and the photon index seems to change as well. However, the $N_{\rm H}$ is clearly compatible with being constant. Finally, we note that the fluxes and the photon indices seem to show some degree of anti-correlation ($r = 0.7$)[1].

2.3. *RXTE*/ASM data

To study the evolution at different timescales of LS 5039 at X-rays, we have analyzed data obtained by the ASM instrument onboard the *RXTE* satellite. The ASM data used here spans from the year 1996 January to 2006 December, or MJD=50094.244–54069.914. Each data point in the original lightcurve represents the fitted source flux of a 90 s pointing or dwell on the source. We note that ASM data are rather poor for faint sources like LS 5039, making time behavior studies difficult due to the relatively small statistics. Moreover, beside the faintness of the source, different technical problems can affect the timing study of the emission, rendering time feature extraction a quite complicated issue. Ribó et al. (1999) and Ribó (2002) carried out a detailed study of LS 5039 ASM data and did not find signifi-

[1] We make a note of caution on these results, accounting for the heterogeneous origin of the data and their treatment.

Table 2. Summary of the results for all the X-ray observations on LS 5039 performed by instruments with imaging capabilities. The unabsorbed fluxes in the energy range 0.3–10 keV, photon indices, and $N_{\rm H}$ (with *wabs* model) values are given. *BeppoSAX* flux errors are the flux dispersion accounting for the count rate changes by a factor of two during the observation and neglecting photon index variations. *ASCA* flux errors are assumed to be a 10% of the flux. The given 2005 *XMM-Newton* $N_{\rm H}$ values are computed with the *wabs* model for comparison with 2003 values. For more details, see Martocchia et al. (2005) (2003 *XMM-Newton* data), Reig et al. (2003) (*BeppoSAX* data), and Yamaoka, K., private communication (*ASCA* data).

Date YYYY-MM-DD	MJD	Mission	Phase range	Flux (0.3–10 keV) $\times10^{-11}$ erg cm^{-2} s^{-1}	Photon index	$N_{\rm H}$ (*wabs*) $\times10^{21}$ cm^{-2}
1999-10-04	51455.9	*ASCA*	0.38–0.47	0.80±0.08	1.6±0.1	7±1
2000-10-01	51818.5	*BeppoSAX*	0.97–0.21	0.5±0.2	1.8±0.2	10^{+3}_{-4}
2002-09-10	52527.3	*Chandra*	0.71–0.73	0.8±0.3	1.1±0.2	6±2
2003-03-08	52706.3	*XMM-Newton*	0.54–0.57	1.03±0.07	$1.56^{+0.02}_{-0.05}$	$7.2^{+0.3}_{-0.5}$
2003-03-27	52725.8	*XMM-Newton*	0.55–0.58	0.97±0.07	$1.49^{+0.05}_{-0.04}$	$6.9^{+0.5}_{-0.3}$
2005-04-13	53473.1	*Chandra*	0.86–0.87	2±1	1.1±0.2	6±1
2005-09-22	53635.8	*XMM-Newton*	0.49–0.53	$1.18^{+0.03}_{-0.07}$	1.51±0.02	6.7±0.2
2005-09-24	53637.8	*XMM-Newton*	0.02–0.05	0.74±0.07	1.59±0.03	6.6±0.2

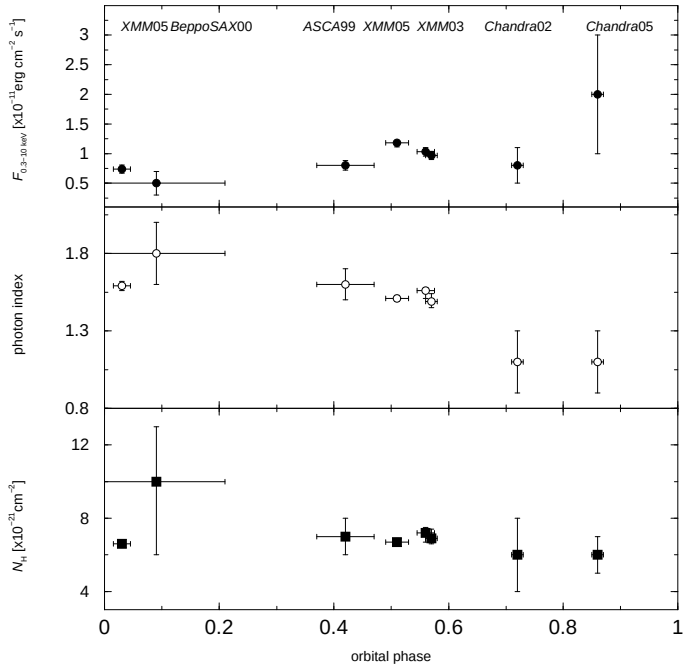

Fig. 5. All observations obtained by X-ray instruments with imaging capabilities folded in orbital phase. At the top, middle and bottom, the 0.3–10 keV unabsorbed flux, the photon index and the $N_{\rm H}$ (with *wabs* model) are presented, respectively. The horizontal error bars represent the duration of the observation.

cant periodicities. In this work, we constrain ourselves to look for possible general trends. The results of this search are presented in Sect. 4 altogether with information obtained at other wavelengths.

3. Hα line observations

We list in Table 3 the journal of optical observations and the corresponding Hα EW. Most of these optical spectroscopic observations of LS 5039 were carried out by us at regular intervals of time between September 2000 and July 2002, with the aim to construct an orbital solution and to monitor the variations of the Hα EW, which would indicate changes in the mass-loss rate of the primary star. A new observing campaign was initiated in 2004 in order to determine the time at which the Hα EW would go above −2.4 Å, the condition required to trigger the 2005 *XMM-Newton* observations.

Various instruments were used in the course of this extended campaign. At the Observatoire de Haute-Provence (OHP), we observed most of the time with the ELODIE Echelle Spectrometer that offers a resolution of 45,000 in the wavelength range 3850–6800 Å. Some additional spectra were obtained with the CARELEC spectrograph (Lemaitre et al. 1990) with a resolution of 900.

At ESO, the majority of the data were acquired with the FEROS Echelle Spectrometer (Kaufer et al. 1999) during the Brazilian time allocation. FEROS offers a resolution of ∼48,000 in the wavelength range 3500–9200 Å. FORS1 observed the source on two occasions with grism GRIS_600V (R=990). The source was also monitored over an orbital cycle with the ESO-NTT and EMMI during a dedicated program in July 2002. The resolution of these spectra obtained with grating #6 in the red arm is 5000. The NTT spectrum obtained in 2005 was acquired through grism #5 with a resolution of 1100. Finally, the spectrum obtained in 1992 is described in Motch et al. (1997).

The spectra obtained on 1999-08-18 and 2004-07-19 were acquired at Osservatorio Astronomico di Bologna with the 1.52 m Loiano telescope and the BFOSC instrument. grism #7 (in 1999) and grism #8 (in 2004) provided a resolution of ∼1600 and 2000 respectively. At the NOT we used the ALFOSC spectrograph with grism #16 and a resolution of ∼3000.

At the Brazilian National Observatory of the Observatório do Pico dos Dias, we used the ESPCASS Cassegrain grating spectrometer mounted on either the 0.6 m or the 1.6 m telescope. The resolving power varies with the observing period from 730 to 3600.

The Hα line has an intrinsic FWHM of ∼8 Å and is therefore relatively well resolved in most of our observations. Due to the southern location of the object, observations from the OHP and Canary Islands were always acquired at a high air mass, typically 1.9 at OHP. At these high air masses, several telluric absorption lines start to be noticeable and can substantially change the value of the Hα EW, either by directly adding to the absorption profile or by changing the value of the reference continuum. These lines are clearly seen in the high resolution ELODIE individual spectra. In the $\lambda\lambda$ range 6540–6580 Å, the most important telluric lines are located at $\lambda\lambda$ 6543.89, 6546.61, 6552.62, 6557.16, 6564.19, 6572.06 and 6574.83 Å. Guided by the atmospheric transmission lines atlas of Hinkle et al. (2003), we could

Table 3. Hα EW measurements obtained from 1992 to 2006*.

Date YYYY-MM-DD	MJD	Orbital phase	Observatory	Instrument	Resolution	Hα EW Å	Error Å
1992-04-19	48731.250	0.85	ESO-2.20	EFOSC2	3,000	−2.80	0.07
1993-06-19	49257.010	0.45	OHP-193	CARELEC	450*	−2.50	0.10
1999-08-18	51408.842	0.35	OAB	BFOSC	1,600	−2.60	0.10
2000-09-08	51795.813	0.42	OHP-193	ELODIE	45,000	−3.24	0.10
2000-09-10	51797.768	0.92	OHP-193	ELODIE	45,000	−2.91	0.15
2000-09-12	51799.768	0.43	OHP-193	ELODIE	45,000	−3.23	0.15
2000-10-18	51835.984	0.70	ESO-1.52	FEROS	48,000	−2.64	0.05
2000-10-19	51836.983	0.96	ESO-1.52	FEROS	48,000	−2.61	0.05
2000-10-20	51838.000	0.22	ESO-1.52	FEROS	48,000	−2.71	0.05
2001-05-24	52053.424	0.37	ESO-VLT-U1	FORS1	990	−2.69	0.07
2001-05-26	52055.417	0.88	ESO-VLT-U1	FORS1	990	−2.69	0.07
2001-08-25	52146.858	0.29	OHP-193	ELODIE	45,000	−2.95	0.10
2001-08-26	52147.857	0.55	OHP-193	ELODIE	45,000	−2.98	0.10
2001-08-28	52149.848	0.06	OHP-193	ELODIE	45,000	−2.91	0.20
2001-08-30	52151.822	0.56	OHP-193	ELODIE	45,000	−2.92	0.20
2001-10-06	52188.978	0.08	ESO-1.52	FEROS	48,000	−2.64	0.10
2001-10-07	52189.992	0.33	ESO-1.52	FEROS	48,000	−2.79	0.10
2001-10-08	52191.050	0.60	ESO-1.52	FEROS	48,000	−2.50	0.15
2001-10-09	52192.000	0.85	ESO-1.52	FEROS	48,000	−2.53	0.10
2002-06-14	52439.340	0.17	ESO-NTT	EMMI	5,000	−2.81	0.05
2002-07-08	52463.335	0.31	ESO-NTT	EMMI	5,000	−2.78	0.05
2002-07-09	52464.141	0.52	ESO-NTT	EMMI	5,000	−2.80	0.05
2002-07-10	52465.052	0.75	ESO-NTT	EMMI	5,000	−2.72	0.10
2002-07-11	52466.214	0.06	ESO-NTT	EMMI	5,000	−2.70	0.05
2004-07-13	53199.923	0.89	OHP-193	CARELEC	900*	−2.60	0.10
2004-07-14	53200.937	0.15	OHP-193	CARELEC	900*	−2.54	0.10
2004-07-16	53202.936	0.66	OHP-193	CARELEC	900*	−2.44	0.10
2004-07-18	53204.906	0.17	OAB	BFOSC	2,000	−2.47	0.10
2004-09-02	53250.935	0.95	LNA-0.60	ESPCASS	1,460	−2.60	0.10
2005-04-07	53467.299	0.34	LNA-1.60	ESPCASS	3,600	−2.83	0.10
2005-04-07	53467.299	0.34	LNA-1.60	ESPCASS	3,600	−2.77	0.10
2005-07-31	53583.748	0.16	ESO-NTT	EMMI	1,100	−2.55	0.05
2005-08-20	53602.935	0.07	LNA-1.60	ESPCASS	2,500	−2.39	0.05
2005-08-20	53602.963	0.08	LNA-1.60	ESPCASS	2,500	−2.34	0.05
2005-08-21	53603.078	0.10	LNA-1.60	ESPCASS	2,500	−2.43	0.05
2005-09-30	53643.005	0.33	LNA-1.60	ESPCASS	730	−2.51	0.10
2006-05-07	53862.181	0.44	NOT	ALFOSC	3,000	−2.40	0.10

* Spectra with EW values corrected for the presence of blended telluric lines.

easily remove the sharp lines due to telluric absorption from the high resolution ELODIE spectra and thus fully correct for atmospheric effects. Some of the FEROS spectra also exhibited evidences of well resolved atmospheric lines at a much lower level than at OHP and could be removed as well.

At a resolution of ∼ 1000 or less, however, atmospheric lines are heavily smeared and cannot be simply removed. They appear as shoulders in the blue and red wings of the broad Hα absorption line of LS 5039 or as slight distortion in the central line profile. We estimated the effect of these lines on the measured equivalent widths by scaling the absorption spectrum of Hinkle et al. (2003) so that they could match the equivalent widths of the narrow lines observed in the mean OHP ELODIE spectrum and applying it to a Gaussian Hα line profile fitting that of LS 5039. Because of the low altitude and relatively high humidity level, the atmospheric effects at OHP are noticeably large. We find that telluric absorptions can easily add 0.4 Å to the equivalent width of a low resolution spectrum at airmass 1.9. Low resolution spectra obtained at OHP were thus rectified using continuum regions clear of known atmospheric lines and their EW were then corrected by 0.4 Å. In the absence of clear measurements or estimates of water vapor column we did not try to correct the other measurements obtained at lower airmasses and under much dryer conditions.

4. Evolution of the X-ray emission, the Hα EW and the radio fluxes

We focus now on the search for possible tendencies on both year and orbital timescales in the evolution of the X-rays and the state of the stellar wind, studying also the long term behavior of the non-thermal radio emission. In addition, we are interested in comparing the behavior of the mentioned source properties (i.e. looking for possible correlations), since it could point out possible physical links between them. For that purpose, we have gathered all the optical data concerning the Hα EW shown in the previous section, plus data presented in previous works (C05: 2003; McSwain et al. 2004: years 1998, 1999, 2000, 2003; Reig et al. 2003: 1999, 2002). Moreover, we have also studied the time evolution of the (total) count rate and hardness ratio ($HR_{B+C/A}$; 3–12 keV: B+C band; 1.5–3 keV: A band) obtained from ASM

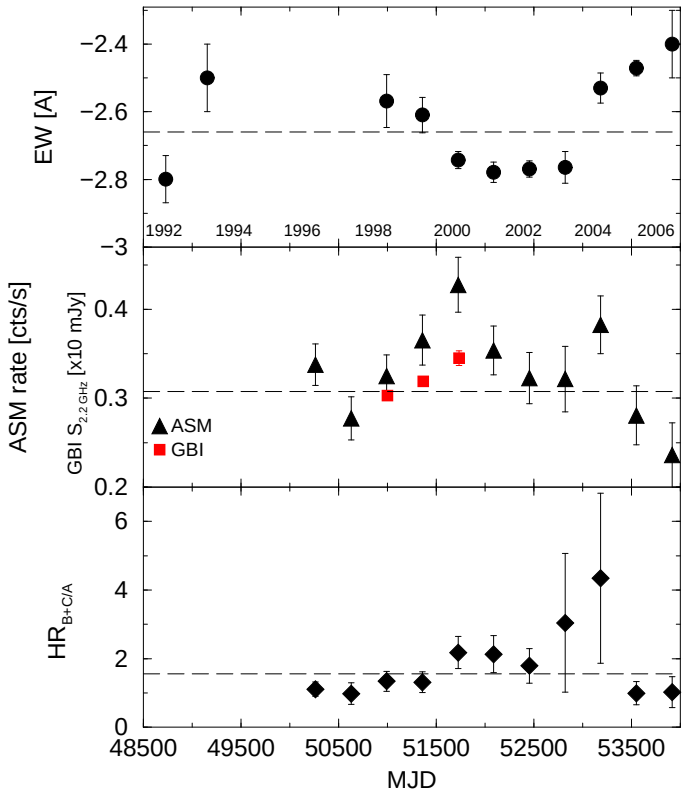

Fig. 6. Top: yearly-averaged curve of the Hα EW. We note that the typical weighted rms bars are $\leq$ 0.1. In some cases, there is only one individual observation per year bin (e.g. 1992, 1993). At the botton of the plot, a year reference is given Middle: yearly-averaged lightcurve for the ASM count rate (black triangles) and the 2.2 GHz GBI flux densities ($\times$10; red squares, errors within symbol). Bottom: yearly-averaged ASM $HR_{B+C/A}$ curve (black diamonds). For comparison, in the three plots the mean value is given (long-dashed line). Due to a lower statistics in the ASM band A, the $HR_{B+C/A}$ error bars for years 2003 and 2004 are larger than for the rest.

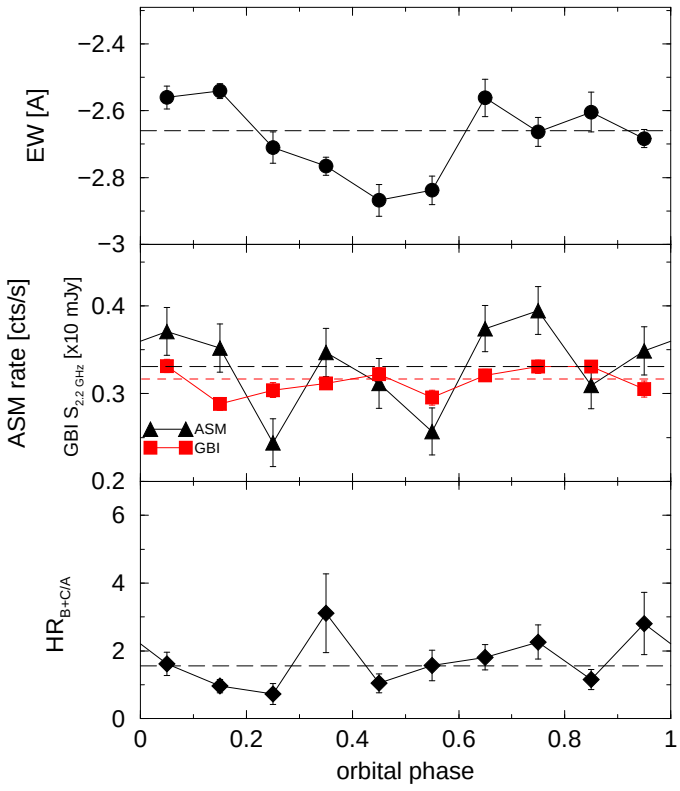

Fig. 7. The same as in Fig. 6 but now the data are folded in orbital phase with bins of 0.1. In the middle plot, the 2.2 GHz GBI mean value is also shown (red dashed line). Due to a lower statistics in the ASM A band, the error bars for phases 0.3–0.4 and 0.9–1.0 are larger than for the rest.

data. Finally, we have revisited here the data taken on LS 5039 by GBI, during the GBI-NASA Monitoring Program in the years 1998–2000, searching for trends at radio frequencies that may be related to those presented by the X-rays or the Hα EW. An accurate analysis of the GBI data were performed by Ribó et al. (1999) and Clark et al. (2001). They found intra-year timescale variability at the level of $\sim$ 20–30% and no periodicities in the GBI data. To create the different curves presented here, we have computed the weighted mean values and errors, using the propagation error method, for the different quantities, averaging per year and folding in orbital phase.

In Fig. 6, the long-term yearly-averaged Hα EW curve (top) and the ASM count rates (middle), are shown. When fitting a constant value to the yearly-averaged curves of both sets of data, we get $\chi^2_{\rm red}$ =14.4 and 2.9 for the Hα EW and the ASM count rate, respectively, thus showing variations, more clear in the former than in the latter. The yearly-averaged Hα EW apparently decreases between the years 1998 and 2000 and increases between the years 2003 and 2006 with a variation of about 10%, which would imply variations in the mass-loss rate by a factor of $\sim$ 2 (see below). The Hα individual observations present strong scattering even when comparing data taken within a year, as can be seen in Table 3 (the typical weighted rms bars are $\sim$ 0.1 Å). The yearly-averaged ASM count rate shows variability of a $\sim$ 80%. The ASM count rate increases between the years 1997 and 2000, and decreases during the years 2004–2006. Comparing the evolution of the ASM count rate and the Hα EW during the years 1998–2006, when data for both is available, an anti-correlation may be suggested, despite the linear correlation coefficient is far from conclusive (r = 0.5). This anti-correlation, if true, would be the opposite to that proposed by Reig et al. (2003)[2].

In Fig. 6 (middle), we show also the yearly-averaged 2.2 GHz fluxes, with a proper re-scaling, taken by GBI. At 8 GHz, the detections are strongly affected by noise, and that is the reason why we show only data at 2.2 GHz, for which detections are at the level of $\sim 8\sigma$ on average (Clark et al. 2001). There is an increase in the 2.2 GHz fluxes between the years 1998 and 2000 by a $\sim$ 20% at a level of 5σ that seems to follow that of the ASM count rate during the same epochs. The Hα EW decreases during these years. We note that the hour angle of the GBI observations changed from -2.3 in 1998–1999 to -0.3 h in 2000, which may affect to some extent the flux average for the latter. It is worth mentioning that Martí et al. (1998) found 5 GHz variability at a level of a 10% on monthly timescales, which is an indication of shorter than year variability of the radio emission.

In Fig. 6 (bottom), the long-term evolution of $HR_{B+C/A}$ is roughly consistent with a constant value ($\chi^2_{\rm red}$ = 1.2). Nevertheless, the evolution of the $HR_{B+C/A}$ seems to show hardening when the ASM count rate increases. This is suggested by the trend of both magnitudes to be above/below the mean value

[2] These authors used pointing X-ray observations, including in their comparison 1998 *RXTE* data that are now known to be background contaminated. Moreover, the relatively small number of available X-ray pointing observations was taken at different orbital phases and could be affected by the additional orbital variability (see Table 2).

at similar epochs, although a correlation cannot be stated from the statistical point of view ($r = 0.5$).

In Fig. 7 (top), the (orbital) phase-folded Hα EW curve in bins of 0.1 in phase is shown. We note that, for observations taken during one orbital period, C05 found no clear trend nor significant variability, and calculated an upper-limit of the stellar mass-loss rate variation of a factor of 2, inferred from the dispersion of the Hα EW value, $\sim 10\%$. The phase-folded curve presented here hints to orbital modulation of the stellar mass-loss rate. A constant fit yields a $\chi^2_{\rm red} = 10.5$, although data are heterogeneous, introducing additional uncertainty.

In Fig. 7 (middle) the ASM phase-folded lightcurve is presented. A constant fit of the phase-folded ASM count rate gives $\chi^2_{\rm red} = 3.4$, suggesting that some kind of variability occurs on these timescales. Although the orbital behavior found by *RXTE*, i.e. X-rays peaking at phase ~ 0.8, is not clearly seen in the phase-folded ASM lightcurve, the ASM data quality is relatively low and spans 11 years of data, precluding a direct comparison. For completeness, we show also here the 2.2 GHz GBI flux curve, with a proper re-scaling folded in phase. A fit to the phase-folded GBI data to a constant renders $\chi^2_{\rm red} = 4.2$. Although the data quality does not allow for an accurate comparison, and the (linear) correlation degree between the GBI and ASM lightcurves is low ($r = 0.4$), a correlation cannot be discarded. The Hα EW and the ASM count rate curves show more correlation, although it is still unclear ($r = 0.6$), and the Hα EW and GBI data show none ($r = 0.2$).

In Fig. 7 (bottom) we have phase-folded the ASM $\rm HR_{B+C/A}$. If the ASM $\rm HR_{B+C/A}$ and count rate are compared, both seem to show a similar trend with respect to their mean values, which may suggest some correlation between them, although it cannot be statistically claimed ($r = 0.5$). Nevertheless, if real, such behavior would be the same as that found in 2003 *RXTE* and 2005 *XMM-Newton* data (see also Fig. 5). When fitting the phase-folded $\rm HR_{B+C/A}$ to a constant value, we get $\chi^2_{\rm red} = 2.1$.

In the context of the Hα and X-ray evolution, it is worth noting that the fluxes measured by *XMM-Newton* in 2005 around phase 0.5 are $\sim 10\%$ marginally larger (2σ) than those found by the same instrument in 2003 (see Table 2). The Hα EW appears also larger by $\sim 10\%$ (3.8σ) when comparing observational results from similar epochs to those of the X-ray ones. These particular results does not favor either a strong positive correlation nor an anticorrelation between the Hα EW and the X-rays.

5. Discussion

5.1. The $N_{\rm H}$ value and the location of the X-ray emitter

Photo-electric absorption in the dense wind of the primary in LS 5039 should increase the observed $N_{\rm H}$ to values above that due to the interstellar medium (ISM) alone. This effect could be detectable when comparing the values of the $N_{\rm H}$ inferred from X-ray and optical observations, respectively. However, the $N_{\rm H}$ values inferred from *XMM-Newton* data (using either *wabs* or *phabs*; see Sect. 2) are similar to, and somewhat smaller than, the value of the ISM $N_{\rm H}$ alone, which is $(7.3 \pm 0.2) \times 10^{21}$ cm^{-2}, derived using the $E_{\rm B-V}$ value from McSwain et al. (2004) and the ISM $N_{\rm H}$-$E_{\rm B-V}$ relationship given by Predehl & Schmitt (1995). In addition, the *XMM-Newton* $N_{\rm H}$ values around phases 0.5 and 0.0 are compatible with being constant, unlike what may be expected given the orbital eccentricity and inclination of the system (see Sect. 1), which should introduce orbital variations in the $N_{\rm H}$ intrinsic to the wind. The 3σ-error of the difference of $N_{\rm H}$ between apastron and periastron is $\approx 10^{21}$ cm^{-2}, which we adopt as an upper-limit to the intrinsic $N_{\rm H}$ variation between these two orbital phases. Taking into account the optical and *XMM-Newton* $N_{\rm H}$ error bars, we take the same value as a conservative upper-limit for the intrinsic $N_{\rm H}$ itself.

To quantify whether the stellar wind can indeed have a negligible impact on the X-ray emission for an emitter located well inside the binary system, we have modeled the wind as spherically symmetric, neglecting X-ray irradiation effects since the modest X-ray luminosity of the source ($\lesssim 10^{34}$ erg s^{-1}) is unlikely to ionize a large fraction of the wind, which could reduce the intrinsic $N_{\rm H}$ value. In fact, we estimate the distance at which X-rays would strongly ionize the wind to be $\lesssim 1/10$ the orbital one (see, e.g., Blondin 1994). To characterize the density of the wind, we have neglected the rotational velocity of the wind, since it is small enough. The radial wind velocity at a distance r from the star has been assumed to follow the law: $V_{\rm w} = V_\infty(1 - R_*/r)^\beta$, where $V_\infty = 2440$ km s^{-1} is the radial velocity of the wind in the infinity, $\beta = 0.8$ is the wind profile exponent, $R_* = 9.3$ R$_\odot$ is the stellar radius and r is the distance to the star (McSwain et al. 2004; C05). The stellar mass-loss rate is taken to be in the range $\dot{M}_{\rm w} \sim 3.7$–7.5×10^{-7} M$_\odot$ yr^{-1} (C05), which allows us to compute the wind density ($\rho_{\rm w}$) through the formula: $\rho_{\rm w} = \dot{M}_{\rm w}/4\pi r^2 V_{\rm w}$. Integrating the wind density from the compact object location along the observer line of sight up to distances where the wind influence is negligible, we obtain an intrinsic $N_{\rm H}$ in the ranges ~ 8–29×10^{21} and ~ 2–5×10^{21} cm^{-2} around phases 0.0 an 0.5, respectively. To look for these minimum and maximum values of the wind $N_{\rm H}$, we have adopted the most extreme values for the inclination and $\dot{M}_{\rm w}$. The $N_{\rm H}$ difference between the two orbital locations is expected to be in the range ~ 3–27×10^{21} cm^{-2}, taking for this comparison the two extreme $\dot{M}_{\rm w}$ values, due to possible orbital variability, but the same i (the one rendering either the smallest or the largest $N_{\rm H}$ difference).

The observed $N_{\rm H}$ seems fairly too low to be composed by an extrinsic ISM plus an intrinsic component as that computed by us. At periastron passage, the intrinsic expected $N_{\rm H}$ value is about one order of magnitude larger than the upper-limit stated above. Even at apastron, the expected intrinsic $N_{\rm H}$ value is several times such upper-limit. Similar disparities are found when comparing the expected intrinsic $N_{\rm H}$ variation between phases 0.5 and 0.0 and the adopted upper-limit. It is worth noting that spherically symmetric wind models seem to work when applied, for instance, to the orbital $N_{\rm H}$ variation in 4U 1538−52 (Mukherjee et al. 2007), an X-ray binary system that presents similar conditions for the absorption along the orbit to LS 5039. Nevertheless, there are some cases in the literature about winds in massive isolated stars that appear to be less dense than expected (e.g. Kramer et al. 2003; Cohen et al. 2006). In these cases, wind clumping has been invoked to explain the low densities of the hydrogen column density inferred from X-ray observations, although a very special wind structure up to $\sim 10\ R_*$ would be required to prevent the observed constancy of the $N_{\rm H}$ for such different orbital phases in LS 5039 if the emitter is well inside the compact object.

The most reasonable scenario seems to be one in which X-rays are emitted at distances at which the stellar wind is already diluted. To reduce the (minimum) differential $N_{\rm H}$ between its two values around phases 0.5 and 0.0 down to the upper-limit given above, it is necessary to locate the emitter away from the compact object. As a typical example, for an emitter on the line subtended by the compact object-observer direction, its location should be at about two orbital radius from the compact object,

i.e. ∼3 and 7×10^{12} cm for periastron and apastron, respectively. A very similar constraint is found for the intrinsic $N_{\rm H}$ value.

5.2. The nature of the X-ray emission and its origin

There are several arguments in favor of a pure non-thermal origin of the emission produced in LS 5039 from soft X-rays to soft gamma-rays. The unabsorbed X-ray spectrum is well explained by a pure power-law, and the data at higher energies obtained by *INTEGRAL* and COMPTEL (De Rosa et al. 2006; Strong et al. 2001; Collmar 2003) do not apparently show a cutoff as it would be expected in a thermal comptonization scenario. We note, nevertheless, that COMPTEL data may be contaminated by other possible sources within the detection error box due to the low angular resolution of the instrument. The probable location of the X-ray source at $\gtrsim 10^{12}$ cm from the compact object, as derived from the absence of $N_{\rm H}$ variation with orbital phase supports the non thermal nature of the high energy emission. An illustrative zoom on the keV–MeV observed spectrum of LS 5039 is presented in Fig. 8. Plausible mechanisms that could produce the keV–MeV spectrum could be synchrotron or inverse Compton processes, although at present they are hard to distinguish without a comprehensive modeling of the multiwavelength radiation produced in the system, being work in progress.

The lack of accretion features, and the apparently non-thermal origin of the X-rays, has been the main argument against the accretion as the powering source in LS 5039, and a young non-accreting pulsar, powering the high energy emission via collision of its wind with the stellar one, has been proposed as the non thermal emitter (see, e.g., Martocchia et al. 2005; Dubus 2006). In such scenario, the extended radio emission would be explained by non thermal particles convected away by the bulk motion of the shocked material, and a compact radio emitting core would be observed located in the system.

It is worth noting that the emission at TeV energies, as in X-rays, does not seem to originate close to the compact object since photon-photon absorption is probably not the dominant effect modulating the TeV emission (Aharonian et al. 2006; Khangulyan et al. 2007). It does not favor a hadronic origin for the TeV radiation either, since the proton-proton interaction efficiency is likely small outside the binary system. In addition, the optically thin nature of the radio emission at least down to ∼ 1 GHz (Martí et al. 1998), and the relatively small radio variability of the core ($\lesssim$ 50%), preclude a too compact emitter. If the multiwavelength emitter is located roughly outside the binary system, the power should be transported efficiently there through some kind of outflow regardless the radiative properties of the launching region. Extended radio emission has been imaged in the range ∼ 1–100 mas, showing an approximately steady orientation of ±15° at different epochs and spatial scales as well as strong collimation (Paredes et al. 2000, 2002). It appears reasonable to associate such extended radio structure with the multiwavelength emitter and the putative outflow. We note that this outflow is likely to be supersonic, since otherwise its dynamics would be dominated by the stellar wind and would hardly be steady and collimated.

In such a context, the particle accelerator could not be too close to the compact object, since the short cooling radiative timescales would prevent accelerated particles to reach the emitting regions. This constraint makes the classical colliding wind scenario less likely since, in that framework, the multiwavelength emission would be mainly generated in the bow shock region, within the binary system (see Dubus 2006). In a jet, in contrast, particle acceleration could take place away from its launching region, since enough kinetic energy could be transported by such a supersonic outflow and converted to non-thermal radiation even outside the binary system. Plausible mechanisms for this conversion are discussed below. Concerning energetics, the jet scenario could be feasible if the observed emission were ultimately powered by accretion (C05), regardless whether the latter shows observational signatures. In any case, the complex radio, X-ray and TeV spectra and lightcurves require deeper modeling. In particular, the lack of clear positive correlation between the Hα EW and the X-ray flux does not favor the classical wind accretion scenario. Whether the jet in LS 5039 is powered by a different accretion process, or it can be explained in the context of a more general young non-accreting pulsar scenario, remains an open question.

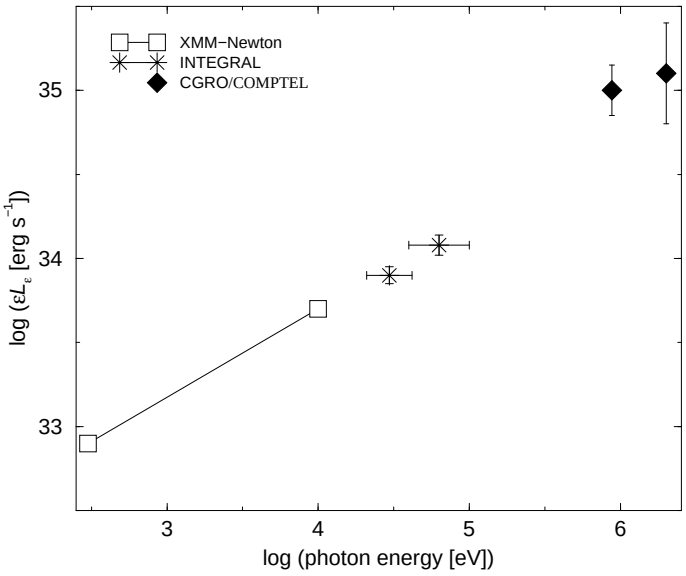

Fig. 8. Spectral energy distribution of LS 5039 from 0.3–3000 keV. *XMM-Newton* data: this work, phase ≈ 0.5; *INTEGRAL* data: De Rosa et al. (2006); COMPTEL data: Collmar et al. (2003).

5.3. Possible jet-wind interactions

Different acceleration mechanisms could be operating at different scales. We focus here on two of them. One possible mechanism could be internal shocks moving through the jet, as it is assumed for blazars (e.g. Rees 1978). In this scenario, the velocities and ejection times of different ejecta should be tuned when modeling such that the shock region would be located at the proper distance from the compact object. An alternative could be interaction with the stellar wind. In this context, a supersonic jet moving at mildly relativistic velocities can become overpressed by the stellar wind. In such a case, strong recollimation shocks (Sanders 1983) can accelerate particles. The location of these recollimation shocks cannot be too close to the compact object, since the jet lateral pressure is very large therein and the jet will expand freely roughly up to the point where lateral pressure balance will be attained with the stellar wind. Assuming the jet is cold and has typical expansion velocities $\lesssim 0.1 V_{\rm jet}$, where $V_{\rm jet} \sim 0.2$ c is the jet velocity (Paredes et al. 2002), and a reasonable jet mass rate of $\sim 10^{-10}$ M$_\odot$ yr^{-1} (e.g. Paredes et al. 2006), lateral ram pressure balance between the jet and the wind in LS 5039 would be attained at $\gtrsim 10^{12}$ cm from the jet origin, locating the accelerator at the binary system borders. One could speculate that the X-ray photon index and flux variations along

the orbit may be related to the changing conditions of the interaction region (e.g. changes in the wind ram pressure, magnetic field, etc.; it may be hinted by the correlation degree between the phase-folded ASM/Hα curves). We note that the dynamical timescales for the wind-jet interaction would be shorter than the orbital period. The details of the jet-wind interaction and the radiative outcomes at different energies are presently under study and will be presented elsewhere.

The annual X-ray flux variations, and the hints of possible ASM/Hα anti-correlation, suggest a link between the X-ray emission and the stellar mass-loss rate. This may also be shared by the radio emission, although it cannot be stated from the present data. In any case, if real, a relationship between the yearly X-ray and Hα EW variability may be linked to the wind-jet interaction, but the complexity of the coupling between the stellar wind and the jet pointed out here precludes presently a straightforward interpretation. It is remarkable that the time, spatial and spectral behavior of the radiation would be much more complex than in the classical disk-jet framework, if powered by shocks propagating through the jet triggered by the wind interaction. These shocks do not necessarily change the main jet properties if this is supersonic and powerful enough to be steady; they could remain as quasi-stationary structures within the flow.

An efficient emitter at $\gtrsim 10^{12}$ cm from the compact object does not preclude that there is radiation of different wavelengths and lower fluxes generated deep inside in the system, in the jet, as well as in a putative accretion disk. For instance, high $N_{\rm H}$ values close to the compact object could mask to some extent thermal X-ray emission in this region. Actually, the main difference between LS 5039 and other microquasars may be the impact of the wind in the jet. This could also explain why the source does not fit the phenomenological radio-X-ray correlation presented by Gallo et al. (2003). It can be argued that other high-mass microquasars have strong winds, like Cygnus X-1, Cygnus X-3 or SS 433. Nevertheless, the X-ray emission in LS 5039 is orders of magnitude dimmer and/or the jet much less powerful, thereby much more exposed to the wind effects.

6. Summary

The 2005 *XMM-Newton* observations of LS 5039 presented here show that the X-ray emission varies slightly in flux and spectral slope between the apastron and periastron passages. However, the hydrogen column density inferred from the X-ray data remains constant within errors between both apastron and periastron runs, and it is even somewhat smaller than the value inferred from the ISM alone, showing that intrinsic absorption is very small, if any. No signatures of a thermal component nor a reflection iron line indicating the presence on a standard accretion disk are present in the data. Intra-hour variations are found when studying the lightcurves, with hints of hardening when the count rate rises. Taken altogether with 2003 *RXTE* and 2005 *Chandra* data, 2005 *XMM-Newton* observations give more grounds to a scenario in which the X-ray flux and photon index vary at orbital (and also shorter) timescales.

We have found strong hints of variability in the yearly-averaged curves of the ASM X-ray count rate and the Hα EW, which may show some degree of anti-correlation in the sense that low X-ray luminosities may appear at times of enhanced stellar mass loss rate. The radio emission (GBI) at 2.2 GHz shows hints of a similar behavior to that of X-rays for the years 1998–2000. The results presented here may suggest also harder spectra at higher count rates for the ASM data, and correlations between the X-rays and the stellar wind at orbital timescales, although it cannot be presently claimed from a statistical point of view.

The low intrinsic absorption inferred from the X-rays in LS 5039, of likely non-thermal origin, can be reasonably explained by locating the X-ray emitter at distances $\gtrsim 10^{12}$ cm from the compact object, as could be also the case for the radio and the TeV radiation. These facts, taken altogether with a possible physical association between the X-ray emission and the stellar wind state, lead us to propose that the dominant multiwavelength non-thermal emission of the source may be produced in a jet interacting with the stellar wind at the borders of the binary system, although deeper modeling is required and the presence of a young non-accreting pulsar in the binary system cannot be at present discarded.

Acknowledgements. We are grateful to M. V. McSwain for providing us with Hα EW information obtained during years 1998, 1999, 2000 and 2003. We thank Dieter Horns and Jennifer R. West for fruitful discussions concerning the analysis of the *Chandra* data presented here. We thank Patrick Guillout, Olivier Herent, Rodrigo P. Campos, M.V.F. Copetti, Laerte Andrade, Adriana Mancini-Pires and Monica M.M. Uchida for conducting part of the optical observations at various observatories. This paper is partially based on quick-look results provided by the ASM/*RXTE* team and data obtained through the HEASARC Online Service of NASA/GSFC. V.B-R. thanks the Max-Planck-Institut für Kernphysik for its support and kind hospitality. M.R. is being supported by a Juan de la Cierva fellowship from the Spanish Ministerio de Educación y Ciencia (MEC). V.B-R., M.R. and J.M.P acknowledge support by DGI of MEC under grant AYA2004-07171-C02-01, as well as partial support by the European Regional Development Fund (ERDF/FEDER). I.N. acknowledges support by DGI of MEC under grant AYA2005-00095. R.L.O. acknowledges financial support from the Brazilian agency FAPESP (grant 03/06861-6). This work is based on observations obtained with XMM-*Newton*, an ESA science mission with instruments and contributions directly funded by ESA Member States and NASA.

References

Aharonian, F., Akhperjanian, A. G., Aye, K. M., et al. 2005, Science, 309, 746
Aharonian, F., Akhperjanian, A. G., Bazer-Bachi, A. R., et al. 2006, A&A, 460, 743
Balucinska-Church, M., & McCammon, D. 1992, ApJ, 400, 699
Blondin, J. M. 1994, ApJ, 435, 756
Bosch-Ramon, V., Paredes, J. M., Ribó, M., et al. 2005, ApJ, 628, 388 (BR05)
Casares, J., Ribó, M., Ribas, I., et al. 2005, MNRAS, 364, 899 (C05)
Clark, J. S., Reig, P., Goodwin, S. P., et al. 2001, A&A, 376, 476
Cohen, D. H., Leutenegger, M. A., Grizzard, K. T., et al. 2006, MNRAS, 368, 1905
Collmar, W., 2003, Proc. 4th Agile Science Workshop, p.177, Frascati (Rome) on 11-13 June 2003
Davis, J. E. 2001, ApJ, 562, 575
de Naurois, M. for the HESS collaboration, Talk presented in the conference: The keV to TeV connection, Rome, October 2006
De Rosa, A., Ubertini, P., Bazzano, A., et al. 2006, AdSpR, proceedings from COSPAR 2006, Ed. Vink, J. & Ghavamian, P., in press [astro-ph/0611114]
Dubus, G. 2006, A&A, 456, 801
Gallo, E., Fender, R. P., & Pooley, G. G. 2003, MNRAS, 344, 60
Goldoni, P., Ribó, M., Di Salvo, T., et al. 2006, Ap&SS, in press [astro-ph/0609708]
Hinkle, K. H., Wallace, L., & Livingston, W. 2003, Bulletin of the American Astronomical Society, 35, 1260
Horns, D. for the HESS collaboration, 2nd Workshop On TeV Particle Astrophysics, Madison, August 2006
Kaufer, A., Stahl, O., Tubbesing, S. et al. 1999, The Messenger, 95, 8
Khangulyan, D., Aharonian, F. A., & Bosch-Ramon, V. 2006, ApJ, submitted
Kramer, R. H., Cohen, D. H., & Owocki, S. P. 2003, ApJ, 592, 532
Lemaitre, G., Kohler, D., Lacroix, D., Meunier, J. P., & Vin, A. 1990, A&A, 228, 546
Martí, J., Paredes, J. M., & Ribó, M. 1998, A&A, 338, L71
Martocchia, A., Motch, C., & Negueruela, I. 2005, A&A, 430, 245
McSwain, M. V., Gies, D. R., Huang, W., et al. 2004, ApJ, 600, 927
Motch, C., Haberl, F., Dennerl, K., Pakull, M., & Janot-Pacheco, E. 1997, A&A, 323, 853
Mukherjee, U., Raichur, H., Paul, B., Naik, S., & Bhatt, N. 2007, [astro-ph/0702142]
Paredes, J.M., Martí, J., Ribó, M., & Massi, M. 2000, Science, 288, 2340

Paredes, J. M., Ribó, M., Ros, E., Martí, J., & Massi, M. 2002, A&A, 393, L99
Paredes, J. M., Bosch-Ramon, V., & Romero, G. E. 2006, A&A, 451, 259
Predehl, P., & Schmitt, J. H. M. M. 1995, A&A, 293, 889
Rees, M. C. 1978, MNRAS, 184, 61
Reig, P., Ribó, M., Paredes, J. M., & Martí, J. 2003, A&A, 405, 285
Ribó, M. 2002, PhD Thesis, Universitat de Barcelona
Ribó, M., Reig, P., Martí, J., & Paredes, J. M. 1999, A&A, 347, 518
Sanders, R. H. 1983, ApJ, 266, 73
Strong, A. W., Collmar, W., Bennett, K., et al. 2001, AIP Conference Proceedings, 587, 21
Torres, D. F., Romero, G. E., Combi, J. A., et al. 2001, A&A, 370, 468
Zavlin, V. E., Pavlov, G. G., Sanwal, D., & Trümper, J. 2000, ApJ, 540, L25